

# A weak-form RBF-generated finite difference method

Mozhgan Jabalameli<sup>a</sup>, Davoud Mirzaei<sup>a,b</sup>

<sup>a</sup>*Department of Applied Mathematics and Computer Science,*

*University of Isfahan, 81746-73441 Isfahan, Iran.*

<sup>b</sup>*School of Mathematics, Institute for Research in Fundamental Sciences (IPM),*

*Tehran 19395-5746, Iran.*

November 30, 2019

## Abstract

In this paper, the idea of direct discretization via radial basis functions (RBFs) is applied on a local Petrov-Galerkin test space of a partial differential equation (PDE). This results in a weak-based RBF-generated finite difference (RBF-FD) scheme that possesses some useful properties. The error and stability issues are considered. When the PDE solution or the basis function has low smoothness, the new method gives more accurate results than the already well-established strong-based collocation methods. Although the method uses a Galerkin formulation, it still remains meshless because not only the approximation process relies on scattered point layouts but also integrations are done over non-connected, independent and well-shaped subdomains. Some applications to potential and elasticity problems on scattered data points support the theoretical analysis and show the efficiency of the proposed method.

**Keywords:** Radial basis functions, Finite difference method, Partial differential equations, Petrov-Galerkin method, Convergence analysis.

**Mathematics Subject Classification (2010):** 65N06, 65N30, 65Dxx, 41Axx.

## 1 Introduction

Radial basis functions (RBFs) are known as a promising tool in approximation theory for reconstructing functions from scattered values. This tool was entered into the field of numerical solution of partial differential equations (PDEs) since a couple of papers by Kansa [16, 17] and continued by many other authors in engineering and sciences. RBFs have advantages of working on scattered points in rather general geometries, being easy

to implement, giving spectral accuracy in some situations, and allowing simple extension to higher dimensions. On the downside, the global RBF approximations produce ill-conditioning matrices which make them restricted for large scale problems. Whereas, the use of local numerical scheme, such as finite differences (FD) yields much better conditioned matrices. Thus, for scattered point layouts a combination of RBFs and FD schemes would be a possible solution. In this direction the RBF-FD approach has been developed for several PDE problems. The earliest reference to this approach seems to be a conference presentation in 2000 [36]. The method then becomes more prevalent in three simultaneous works [34, 37, 41] in 2003. As in the classical FD methods, RBF-FD results in sparse matrices with an additional advantage that has all the flexibility of global RBFs in terms of handling irregular geometries and scattered node layouts. Although the RBF-FD method does not perform the same spectral accuracy (for example for Gaussian) as global RBF scheme, it will give acceptable accuracy for large scale problems for which the global RBF can not be implemented.

The RBF-FD method still requires an appropriate algorithm to avoid the ill-conditioning at the *near flat* cases, i.e. for very small values of RBF shape parameters [11, 10, 8, 18, 12]. Equipping with such algorithm, the RBF-FD method has been successfully applied on a large class of PDEs in Euclidian spaces and smooth sub-manifolds [6, 9, 7].

The *testing strategy* in all the previous studies is a simple *collocation* approach where the test space is discretized by collocating the strong form of the PDE at a set of scattered test points. In this paper we will use an alternative approach based on a *local Petrov-Galerkin* test discretization. The PDE is first converted to a weak form over not the global domain but some small subdomains around the scattered test points, leading to a set of *local weak-form test functionals* instead of the known *delta point evaluations* of the collocation method. The procedure then follows the same direction as the usual RBF-FD methods. At the price of numerical integration, the new method requires lower order derivatives of the RBF space leading to better convergence properties. In additions, the method is applicable on PDE problems with low smooth solutions because the information of the right-hand side function (source function) should only be available in a weak sense. Moreover, a *scaling property* of the weak-form functionals allows to implement the new method via *polyharmonic spline* RBFs in a stable and efficient way. Alongside, the available stabilization techniques for other RBFs such as RBF-QR and RBF-RA are still applicable in the new procedure.

Although the new method is based on a Galerkin formulation, there is a significant improvement over some meshless Galerkin methods (such as element-free Galerkin (EFG) method) that no triangulation or background mesh is needed for numerical integration. In fact, in the new method integrations are done over non-connected, independent and well-shaped subdomains. This means that no connected background mesh is required for either approximation or integration.

The reminder parts of the paper are organized as following. In section 2, an overview

on meshless methods and two different approaches for solving PDEs are reviewed. In section 3, a local Petrov-Galerkin test discretization of a PDE problem is derived. In section 4, the idea of RBF-FD approach is developed for the new testing functionals and the available algorithms for stabilizing the resulted local matrices are reviewed. In section 6, the theoretical foundation of the method is provided and the consistency and stability issues are considered. Finally, in section 7, some applications to potential and elasto-static problems with numerical experiments are given.

## 2 An overview

Assume that we are looking for the approximate solution of a PDE problem of the form

$$Lu = f, \quad \text{in } \Omega, \quad (2.1)$$

$$Bu = g, \quad \text{on } \Gamma \quad (2.2)$$

where  $\Omega$  is a domain in  $\mathbb{R}^d$ ,  $\Gamma = \partial\Omega$  denotes its boundary,  $L$  is a linear differential operator,  $B$  is a linear boundary operator describing the Dirichlet and/or Neumann boundary conditions. Meshless methods construct the approximate solution from a *trial space* whose functions are parametrized “entirely in terms of nodes”. If *trial points* form a set

$$Z = \{z_1, z_2, \dots, z_M\}$$

then we denote the trial space by  $U_Z$  and assume that the discretized problem is set up with a vector  $(u(z_1), u(z_2), \dots, u(z_M))^T$ . Furthermore, we assume the discretized problem consists of *test functional* equations

$$\lambda_k u = b_k, \quad k = 1, \dots, N, \quad (2.3)$$

where we have  $N \geq M$  linear functionals  $\lambda_1, \dots, \lambda_N$  and  $N$  prescribed real values  $b_1, \dots, b_N$ . In collocation methods, test functionals  $\lambda_k$  are simply formed by values of  $Lu$  and  $Bu$  at collocation points  $x_1, \dots, x_N$  in  $\Omega$  and  $\partial\Omega$ , respectively. Correspondingly,  $b_k$  are  $f$  and  $g$  values. In section 3 we will describe an alternative discretization technique to convert (2.1)-(2.2) into semi-discrete form (2.3).

For discretization in the trial side, a standard approach uses the expansion

$$\tilde{u} = \sum_{j=1}^M a_j u(z_j) \approx u$$

of the approximate solution in terms of a set of shape functions  $\{a_1, \dots, a_M\}$  as a Lagrange basis for trial space  $U_Z$ . Applying  $\lambda_k$  then yields

$$\lambda_k \tilde{u} = \sum_{j=1}^M \lambda_k a_j u(z_j) \approx \lambda_k u, \quad k = 1, \dots, N$$

which describes the exact action of test functionals  $\lambda_k$  on the trial space. Putting the  $\lambda_k a_j$  into an  $N \times M$  matrix  $A$ , one has to solve the possibly overdetermined linear system  $A\mathbf{u} = \mathbf{b}$  with  $\mathbf{b} = (b_1, \dots, b_N)^T$ . Since “ $\approx$ ” is replaced by “ $=$ ” to end up with the final system, the vector value  $\mathbf{u}$  may differ from nodal values  $(u(z_1), \dots, u(z_M))^T$ . This approach which is called the *shape function approach* in [32] dominates all classical collocations and FEM types methods. In kernel based methods, unsymmetric and symmetric collocation methods [13, 29, 43] as well as Galerkin RBF based methods [39, 24, 19] are examples that use this approach. A general and comprehensive error and stability analysis is also provided in [32].

An alternative approach, having FDM as an example, finds good estimates  $\tilde{\lambda}_k$  of all  $\lambda_k$  by looking for real numbers  $a_j(\lambda_k)$  with

$$\tilde{\lambda}_k u = \sum_{j=1}^M a_j(\lambda_k) u(z_j) \approx \lambda_k u, \quad k = 1, \dots, N \quad (2.4)$$

to get a different linear system  $A\mathbf{u} = \mathbf{b}$  with matrix entries  $a_j(\lambda_k)$  and the same  $\mathbf{b}$  as before. Usually  $A$  is a sparse matrix in this case. This approach is called *direct discretization* in [30] because test functionals  $\lambda_k$  are directly approximated from nodal values  $u(z_1), \dots, u(z_M)$  without any detour via shape functions. It has been also used in meshless methods like RBF-FD, local RBF collocation and generalized moving least squares (GMLS) approximation by various authors [36, 34, 7, 25, 23, 30].

The method of this paper is of the second type and generalizes the FD methods for weak-form functionals on scattered points using a special Petrov-Galerkin test discretization and the RBF approximation.

### 3 Locally weak testing

The usual classification of numerical methods for solving a PDE obeys the classification of PDE problem itself into *strong* and *weak* forms. The first yields the standard collocation methods, while the second dominates all FEM and related techniques. However, there exists an alternative approach, originally proposed in [1] as *local weak* form, which splits the integral of the usual global weak form into local integrals over many small subdomains and performs the integration by parts on all local integrals, separately.

Any such above forms constructs a testing space for the PDE and converts it to a finite set of functional equations as (2.3). On the other side, the trial space is usually formed via piecewise polynomials, orthogonal polynomials, spline functions, trigonometric polynomials, moving least squares (MLS), RBFs, and etc.

In this section we derive the local weak forms associated to linear PDE problem (2.1)-(2.2). Assume

$$X = \{x_1, x_2, \dots, x_{n_X}\}$$

is a set of *PDE test points* inside  $\Omega$  and

$$Y = \{y_1, y_2, \dots, y_{n_Y}\}$$

is a set of *boundary test points* on  $\Gamma$ . Let  $N = n_X + n_Y$  is the number of all test points. Moreover, assume  $v : \mathbb{R}^d \rightarrow \mathbb{R}$  is a compactly supported test function on the unit ball and for  $x = x_k \in X$  define

$$v_{\rho,x} := \rho^{-d} v \left( \frac{\cdot - x}{\rho} \right), \quad (3.1)$$

where  $\rho > 0$  is chosen small enough to have  $B(x_k, \rho) \subset \Omega$  for all  $k = 1, 2, \dots, n_X$ . In contrast to the well-established Galerkin methods which are based on a global weak form, we introduce the *local weak forms* of (2.1) by integrating  $Lu$  against test functions  $v_{\rho,x_k}$  to get

$$\langle Lu, v_{\rho,x_k} \rangle_{L_2(\Omega)} = \langle f, v_{\rho,x_k} \rangle_{L_2(\Omega)}, \quad k = 1, 2, \dots, n_X.$$

Integration by parts and using the divergence theorem on the left hand side then weaken the strong form  $L$  to lower order derivatives of the function involved. For instance, the local weak forms of the well-known Laplacian operator  $L = \Delta$ , using the fact that  $v_{\rho,x_k}$  is compactly supported on  $B = B(x_k, \rho) \subset \Omega$ , read as

$$\langle \nabla u, \nabla v_{\rho,x_k} \rangle_{L_2(B)} - \langle \nabla u \cdot n^{(k)}, v_{\rho,x_k} \rangle_{L_2(\partial B)} = \langle f, v_{\rho,x_k} \rangle_{L_2(B)} \quad (3.2)$$

where  $n^{(k)} \in \mathbb{R}^d$  is the outward normal to the boundary of ball  $B(x_k, \rho)$ , i.e.

$$n^{(k)}(x) = \frac{x - x_k}{\rho}.$$

Another example of local weak forms will be given in section 7 for an elasticity problem in solid mechanics.

Test functions  $v$  are chosen independently of trial functions, the reason why we call (3.2) a Petrov-Galerkin discretization. Two simple choices of  $v$  are as follows: 1) If  $v$  is vanishing on  $B(0, 1)$  then the second inner product in the left hand side of (3.2) vanishes. Wendland's compactly supported RBFs (see Table 1) are examples. 2) If  $v$  is the constant function on set  $B(0, 1)$  and zero otherwise, i.e.  $v = \chi_{B(0,1)}$ , then the second inner product is vanishing and we have a local boundary-only integral.

It is clear from the construction that local subdomains may have other shapes than balls if the corresponding test functions  $v_{\rho,x_k}$  are defined properly.

In general, for a given test function  $v$ , we show the local weak forms of (2.1) by

$$a_{\rho,k}(u, v) = \ell_{\rho,k}(v), \quad k = 1, 2, \dots, n_X, \quad (3.3)$$

for unknown solution  $u$ , where  $a_{\rho,k}$  are local bilinear forms and  $\ell_{\rho,k}$  are local linear functionals. Allowing local subdomains  $B(x_k, \rho)$ ,  $k = 1, \dots, n_X$  to be independent from each

other (with or without intersection) and extending the support of approximant outside these subdomains make the bilinear form (3.3) different from the usual Petrov-Galerkin discretizations in the FEM setting where meshes (e.g. triangles) do not overlap and their union should cover the whole domain  $\Omega$ .

For boundary test points  $y_k \in Y$  we introduce the collocation test functional equations

$$(\delta_{y_k} \circ B)u = g(y_k), \quad k = 1, 2, \dots, n_Y, \quad (3.4)$$

where  $\delta_y$  is the point evaluation functional at  $y$ .

We now define for a given  $v$  and  $\rho$

$$\begin{aligned} \lambda_k u &:= a_{\rho,k}(u, v), \quad k = 1, \dots, n_X, \\ \lambda_{k+n_X} u &:= \delta_{y_k} \circ B(u), \quad k = 1, \dots, n_Y, \end{aligned} \quad (3.5)$$

and

$$\begin{aligned} b_k &:= \ell_{\rho,k}(v), \quad k = 1, \dots, n_X, \\ b_{k+n_X} &:= g(y_k), \quad k = 1, \dots, n_Y, \end{aligned} \quad (3.6)$$

to arrive at the semi-discrete form (2.3). If the first approach of section 2 (the shape function approach) is applied on this test discretization then the well-known MLPG method will be resulted where shape functions are usually coming from the moving least squares (MLS) and RBF approximations [1, 24]. However, as pointed out before, we are going to follow the second approach and give a stable and robust numerical scheme to transfer the problem to a full-discrete linear system of equations.

## 4 RBF-generated FD method

The RBF-FD method arises naturally as a generalization of standard FD approximations. FD formulas approximate a differential operator at a central point  $x_0$  in terms of function values at distinct points  $z_1, z_2, \dots, z_n$  in neighborhood of  $x_0$ . These formulas are usually derived only in one dimension by considering the stencil weights to be unknowns and then enforce that the resulting FD formula becomes exact for the monomials  $1, x, x^2, \dots$  up to as high degree as possible. Generalizations to more dimensions are mostly limited to Cartesian-type grids by applying such one dimensional formulas in each spatial direction, separately. In RBF-FD approach the one dimensional test functions  $\{1, x, x^2, \dots\}$  are replaced by  $d$  dimensional RBFs  $\{\phi(\|x - z_j\|_2)\}$  centered at nodes  $z_j \in \mathbb{R}^d$ ; usually no matter how they are scattered. In certain cases, low-degree polynomials have to be added, but we give details later. The basis function  $\phi$  is assumed to be (conditionally) positive definite.

**Definition 4.1** *A continuous radial function  $\phi$  is conditionally positive definite of order  $q$  on  $\mathbb{R}^d$  if*

$$\sum_{i=1}^n \sum_{j=1}^n c_i c_j \phi(\|z_i - z_j\|_2) > 0$$

Table 1: Typical RBFs for  $r = \|x\|_2$ ,  $x \in \mathbb{R}^d$ .

RBF	$\phi(r)$	Parameters	Order $q$
Gaussian	$\exp(\varepsilon^2 r^2)$	$\varepsilon > 0$	0
Sobolev spline	$r^{\beta-d/2} K_{\beta-d/2}(\varepsilon r)$	$\beta > d/2, \varepsilon > 0$	0
IMQ	$(1 + \varepsilon^2 r^2)^{-\beta}$	$\beta > 0, \varepsilon > 0$	0
MQ	$(1 + \varepsilon^2 r^2)^\beta$	$\beta > 0, \beta \notin \mathbb{N}, \varepsilon > 0$	$\lceil \beta \rceil$
Polyharmonic splines (PHS)	$\begin{cases} r^k \log r \\ r^k \end{cases}$	$\begin{cases} k \in 2\mathbb{N} \\ k \notin 2\mathbb{N}, k > 0 \end{cases}$	$\lfloor k/2 \rfloor + 1$
Wendland's functions	$\phi_{d,k}(\varepsilon r)$	$k \in \mathbb{N}_0, d \in \mathbb{N}, \varepsilon > 0$	0

for any  $n$  pairwise distinct points  $z_1, z_2, \dots, z_n \in \mathbb{R}^d$  and any vector  $c = [c_1, c_2, \dots, c_n]^T \in \mathbb{R}^n$  satisfying the side condition

$$\sum_{j=1}^n c_j p(z_j) = 0, \quad \text{for all } p \in \mathbb{P}_{q-1}^d.$$

Function  $\phi$  is called *positive definite* if it is *conditionally positive definite* of order  $q = 0$ .

Typical examples of RBF  $\phi(r)$  for  $r = \|x\|_2$ ,  $x \in \mathbb{R}^d$ , are listed in Table 1. In the second row of the table,  $K_\beta$  is the modified Bessel function of the second kind of order  $\beta$ . Shape parameter  $\varepsilon > 0$  plays an important role in accuracy and stability of RBF approximations. Polyharmonic splines (PHS) are examples of  $\varepsilon$ -free RBFs. For explicit formula of Wendland's functions  $\phi_{d,k}(\varepsilon r)$  see [38].

Although, FD formulas are usually constructed to approximate the strong derivatives and hence FDM is known as a strong-based method, here we derive the weak-based RBF-FD formulas based on our special Petrov-Galerkin test discretization in section 3. This might be a little unfamiliar at first glance, but as we discussed in section 2 and we will see below, the *direct approximation* of linear functionals without operating them on a trial space, push this method to the category of FD methods.

We again assume  $Z = \{z_1, z_2, \dots, z_M\}$  is a set of trial points distributed in  $\Omega$  and on  $\Gamma$  and  $X = \{x_1, \dots, x_{n_X}\}$  is a set of PDE test points inside  $\Omega$ . Recall the local bilinear forms  $a_{\rho,k}(u, v) =: \lambda_k u$  corresponding to test points  $x_k$  from (3.3). This functional values can be *directly* and locally approximated by values of  $u$  at a subset of trial set point  $Z$  nearing  $x_k$ . This can be done by computing an RBF-generated stencil for  $n_k$  points from  $Z$  locating in neighborhood of  $x_k$  denoted by  $Z_k = Z \cap B(x_k, \delta)$  for  $\delta > \rho$ . In doing so, we are looking for weights  $w^{(k)} = (w_1^{(k)}, w_2^{(k)}, \dots, w_{n_k}^{(k)})^T$  such that for a fixed test function  $v$ ,

$$a_{\rho,k}(u, v) \approx w^{(k)T} u|_{Z_k}$$

where the test point  $x_k$  is assumed to be located approximately at the center of stencil. By  $u|_{Z_k}$  we mean the vector of nodal values at  $Z_k$ . To obtain the weight vector  $w^{(k)}$ , we require the stencil to reproduce all functions spanned by the involved RBFs  $\{\phi(\|\cdot - z_j\|_2)\}_{z_j \in Z_k}$ . It happens if  $w^{(k)}$  satisfies

$$\sum_{z_j \in Z_k} w_j^{(k)} \phi(\|z_j - z_i\|_2) = a_{\rho,k}(\phi(\|\cdot - z_i\|_2), v), \quad z_i \in Z_k, \quad (4.1)$$

or in matrix form

$$A_\phi^{(k)} w^{(k)} = b_{\rho,\phi}^{(k)}. \quad (4.2)$$

If  $\phi$  is positive definite then (4.2) is uniquely solvable. It is beneficial to also augment the stencil with polynomial terms and add matching constraints to the associated RBF expansion coefficients. This corresponds to requiring the weights to further reproduce the polynomial space  $\mathbb{P}_{q-1}(\mathbb{R}^d) = \text{span}\{p_1, \dots, p_Q\}$  where  $Q = \binom{q-1+d}{d}$ . The augmented linear system then becomes

$$\begin{bmatrix} A_\phi^{(k)} & P^{(k)} \\ P^{(k)T} & 0 \end{bmatrix} \begin{bmatrix} w^{(k)} \\ \nu^{(k)} \end{bmatrix} = \begin{bmatrix} b_{\rho,\phi}^{(k)} \\ c^{(k)} \end{bmatrix}, \quad (4.3)$$

where  $P_{j,i}^{(k)} = p_i(z_j)$ ,  $z_j \in Z_k$ ,  $1 \leq i \leq Q$  and  $c_i^{(k)} = a_{\rho,k}(p_i, v)$ . As a sufficient condition, the solvability of (4.3) is guaranteed if  $\phi$  is conditionally positive definite of order  $q$  in  $\mathbb{R}^d$  and  $Z_k$  is a  $\mathbb{P}_{q-1}(\mathbb{R}^d)$ -unisolvent set.

**Definition 4.2** *A finite point set  $Z \subset \mathbb{R}^d$  is  $\mathbb{P}_m^d$ -unisolvent if the zero function is the only polynomial from  $\mathbb{P}_m^d$  that vanishes on  $Z$ . Equivalently,  $Z$  has polynomial reproduction of order  $m + 1$  (or degree  $m$ ).*

After solving (4.3), we can safely ignore the weight vector  $\nu^{(k)}$  and use only  $w^{(k)}$  to form the  $k^{\text{th}}$  stencil.

The same can be done for the boundary test functional (3.4) by replacing the right hand side of (4.1) by strong functional values

$$(\delta_{y_k} \circ B)\phi(\|\cdot - z_i\|_2)$$

for differential boundary operator  $B$  that will only change the right hand side of (4.2) or (4.3).

The PDE problem (2.1)-(2.2) is now discretized to the final linear system

$$A\mathbf{u} = \mathbf{b} \quad (4.4)$$

for unknown vector  $\mathbf{u} \in \mathbb{R}^M$  which is the approximate vector value at trial points  $z_1, \dots, z_M$ . Matrix  $A \in \mathbb{R}^{M \times N}$  is a sparse matrix assembled by the computed stencil weights; the  $k^{\text{th}}$  row of  $A$  is formed via  $w^{(k)T}$  together with many zeros corresponding to points in  $Z \setminus Z_k$ . Note that in a practical computation, we do not actually store the whole

$A$  but only its nonzero entries. The right hand side vector  $\mathbf{b} \in \mathbb{R}^N$  has entries  $b_k = \ell_{\rho,k}(v)$  for  $k = 1, \dots, n_X$ , and  $b_{n_X+k} = g(y_k)$  for  $k = 1, \dots, n_Y$ .

For postprocessing calculations, the approximate values of  $u$  and its derivatives at any *evaluation* point  $x \in \Omega$  can be obtained by calculating the stencil weight  $w^{(eval)}$  and computing the inner product of its zero extension with  $\mathbf{u}$ .

In section 6, the convergence and stability properties of this method will be discussed but before that we consider the conditioning of local systems (4.2) and (4.3) in the following section.

## 5 Ill-conditioning of local systems

Although the method uses the RBF space on local subdomains to construct the stencil weights, it still suffers from the severe ill-conditioned local interpolation matrices for nearly flat  $\varepsilon$ -dependent RBFs for which the results tend to become particularly accurate. It happens when the shape parameter  $\varepsilon$  is chosen very small. On the other side, for  $\varepsilon$ -free RBFs (such as PHS) if the stencil (with a fixed number of points) becomes localized around the central point then the local system tends to be highly ill-conditioned. This problem occurs in the intermediate step when the stencil weights are calculated via (4.2) or (4.3) for different test points. The sparse final linear system (4.4) is well-conditioned and can effectively be inverted for a large number of points.

As we know, the standard RBF interpolation works with basis

$$\{\phi(\|\cdot - z_1\|_2), \phi(\|\cdot - z_2\|_2), \dots, \phi(\|\cdot - z_n\|_2)\} \quad (5.1)$$

on trial point set  $Z$ . For infinitely smooth functions such as Gaussian, IMQ and MQ the growth of the condition number of  $A_\phi$  depends exponentially on the decay of both shape parameter  $\varepsilon$  and separation distance  $q_Z = \min_{k \neq j} \|z_k - z_j\|$ . For finitely smooth RBFs this dependence is of algebraic order. See [40, Chapter 12] for proofs. However, it is well-known that the RBF interpolants are best approximations in *native spaces* [40, Chapter 10]. This means the interpolation operator is stable (at least) in the native space norm. For finitely smooth basis functions with Fourier transforms decaying only algebraically, DeMarchi and Schaback [22] proved that the RBF interpolations are stable even in  $L_2$  and  $L_\infty$  norms. (The same proof for infinitely smooth RBFs is still an open problem!). These all show that *stable basis* may exist. In this direction, for the Gaussian basis function the RBF-QR [11, 8] and the RBF-GA [10] algorithms have been introduced to handle the flat limit cases at the price of a more computational cost. See also [27, 28, 20, 21] for new bases for RBF spaces.

However, the first attempt to avoid the instability for small values of  $\varepsilon$  (applicable for all types of RBFs) may be referred to the Contour-Padé algorithm which does not change the basis (5.1) but extends the computation of interpolant to complex values of  $\varepsilon$  on a

safe path. The use of *Padé* approximation then allows to approximate the interpolant at small real values of  $\varepsilon$  [12, 41]. This algorithm was significantly improved to RBF-RA version in [42] where the vector-valued rational interpolation is used instead of the Padé approximation.

Another approach uses the scalability and allows to construct optimal stencils in Sobolev spaces stably and efficiently [4]. If both functional and nodal approximation are scalable then computations can be carried out with a proper scaling parameter and finally re-scaled to the original situation. This may be motivated by the five-point star classical FD formula for  $\Delta u$  at origin on points  $Z = \{(0, 0), (1, 0), (-1, 0), (0, 1), (0, -1)\} \subset \mathbb{R}^2$  with weights  $w = \{4, -1, -1, -1, -1\}$ . If points are scaled to

$$hZ = \{(0, 0), (h, 0), (-h, 0), (0, h), (0, -h)\}, \quad h > 0$$

then weights are scaled to  $w/h^2 = \{4/h^2, -1/h^2, -1/h^2, -1/h^2, -1/h^2\}$ . Here 2 is the scaling order of  $\Delta$ . This scaling order also determines the convergence rate of the formula. In the RBF context, this approach is applicable for PHS on scattered points and excludes other well-known kernels. However, in [4] has been proved that scalable stencils constructed via PHS provide optimal convergence rates in Sobolev spaces. See section 6 below.

Comparing with the strong-based RBF-FD method, since matrices  $A_\phi^{(k)}$  and  $P^{(k)}$  remain unchanged in the new formulation, the stabilization algorithms for  $\varepsilon$ -dependent RBFs (such as RBF-QR and RBF-RA) can be easily modified for systems (4.2) and (4.3). However, for PHS kernels the *scaling rule* of the new test functionals needs to be determined beforehand. See equation (6.6) of the following section.

## 6 About the convergence analysis

Assume the PDE problem (2.1) together with boundary condition (2.2) possess a unique true solution  $u^*$  that lies in some regularity subspace  $U$  that carries a norm  $\|\cdot\|_U$ . According to the outlined test discretization of section 3 we have

$$\lambda_k u^* = b_k, \quad k = 1, 2, \dots, N \tag{6.1}$$

where  $\lambda_k$  and  $b_k$  are defined via (3.5) and (3.6), respectively. As discussed in section 4, the method of this paper approximates each functional  $\lambda_k u^*$  by linear combinations of nodal values  $u^*(z_1), \dots, u^*(z_M)$  by requiring

$$\lambda_k u^* \approx \sum_{z_j \in Z_k} w_j^{(k)} u^*(z_j) =: \tilde{\lambda}_k u^*, \quad k = 1, \dots, N.$$

Comparing with (2.4) of section 2, we have  $a_j(\lambda_k) = w_j^{(k)}$  for  $\{j : z_j \in Z_k\}$  and  $a_j(\lambda_k) = 0$  otherwise. Thus, the method leads to a sparse and possibly overdetermined final lin-

ear system (4.4) for  $\mathbf{u} = (u_1, \dots, u_M)^T$  if we let the true values  $u^*(z_j)$  be replaced by approximate values  $u_j$ .

The error analysis of this method falls into a framework of Schaback for nodal meshless methods [31]. Since the square system of certain meshless methods may be singular, one can apply *overtesting*, i.e. choosing  $N$  (the number of test points) larger than  $M$  (the number of trial points), to avoid singularity and to improve the stability [32]. The resulting overdetermined linear system of equations then should be handled by standard numerical linear algebra techniques. For solvability we assume that the matrix  $A$  is set up by sufficiently thorough testing so that the matrix has rank  $M \leq N$ .

As well as any numerical PDE method, the *consistency* and the *stability* together with the effect of the *numerical linear algebra solver* are three ingredients that determine the convergence quality of this method. The consistency is analyzed by finding a sharp upper bound for

$$\|A\mathbf{u}^* - \mathbf{b}\|_q$$

where  $\|\cdot\|_q$  is the discrete  $q$ -norm in  $\mathbb{R}^N$ , i.e.  $\|\mathbf{v}\|_q^q := |v_1|^q + \dots + |v_N|^q$  for  $\mathbf{v} = (v_1, \dots, v_N)^T \in \mathbb{R}^N$ . For this we assume there is a consistency error bound

$$|\lambda_k(u^*) - \tilde{\lambda}_k(u^*)| \leq \tau_k \|u^*\|_U, \quad k = 1, 2, \dots, N, \quad (6.2)$$

to get

$$\|A\mathbf{u}^* - \mathbf{b}\|_q \leq \|\boldsymbol{\tau}\|_q \|u^*\|_U.$$

Suppose  $\hat{\mathbf{u}}$  denotes the vector of approximate nodal values  $\hat{u}_j$  that is obtained by some numerical linear algebra method that solves the system (4.4) approximately. Then, we assume

$$\|A\hat{\mathbf{u}} - \mathbf{b}\|_q \leq K(A) \|A\mathbf{u}^* - \mathbf{b}\|_q \leq K(A) \|\boldsymbol{\tau}\|_q \|u^*\|_U, \quad (6.3)$$

which is a condition imposed by the numerical method that produces  $\hat{\mathbf{u}}$ . Note that (6.3) can be obtained with  $K(A) = 1$  if  $\hat{\mathbf{u}}$  is calculated via minimization of the residual  $\|A\mathbf{u} - \mathbf{b}\|_q$  over all  $\mathbf{u} \in \mathbb{R}^M$ . Finally, for stability we define

$$C_S(A) := \sup_{\mathbf{u} \neq 0} \frac{\|\mathbf{u}\|_p}{\|A\mathbf{u}\|_q} \quad (6.4)$$

which is a finite constant for any  $q$  and  $p$  norms provided that  $A$  has no rank loss. Having these, Schaback [31] proved the following theorem which gives an error bound at nodal points.

**Theorem 6.1** *Under the above assumptions and notations we have*

$$\|\mathbf{u}^* - \hat{\mathbf{u}}\|_p \leq (1 + K(A)) C_S(A) \|\boldsymbol{\tau}\|_q \|u^*\|_U.$$

This is a classical error analysis where the right hand side contains the product of the stability constant and the consistency bound. The effect of the linear algebra solver is also reflected by constant  $K(A)$ .

## 6.1 Consistency

First, we focus on the consistency error bound (6.2) and use the results of Davydov and Schaback [3, 4] among a large list of sources concerning the error analysis of kernel based approximations. In [3] an error bound for kernel based numerical differentiation is provided using the new technique of *growth function*. This technique bypasses certain point density assumptions that were needed in standard approach of estimating the error in terms of the fill distance. Thus it is more suitable to apply on stencils where the number of points is more important than having a sufficiently dense point set.

Before measuring the consistency and the stability bounds of the new method, let's introduce some notions and notations.

A domain  $\Omega \subset \mathbb{R}^d$  is *scalable*, if it contains the origin as an interior point and satisfies  $h\Omega \subseteq \Omega$  for all  $0 \leq h \leq 1$ , i.e. if  $\Omega$  is star-shaped with respect to the origin. A space  $U$  of functions on a scalable domain  $\Omega$  is scalable, if  $u(h\cdot)$  is in  $U$  for all  $0 < h \leq 1$  and all  $u \in U$ . A functional  $\lambda \in U^*$  on a scalable space  $U$  has *scaling order* or homogeneity order  $s$  if

$$\lambda(u(h\cdot)) = h^s \lambda(u), \text{ for all } u \in U. \quad (6.5)$$

For example we can simply show that the standard strong functional  $\lambda(u) = D^\alpha u(0)$  has scaling order  $s = |\alpha|$ .

More calculations are required to determine the scaling order of local weak form functionals of this paper. As an example, if  $v_{\rho,x}$  is defined via (3.1) for a test function  $v \in H^1(\mathbb{R}^d)$  with a compact support on  $B(0, 1)$  and vanishing on  $\partial B(0, 1)$ , we have

$$\begin{aligned} \lambda_{v_{\rho,x}}(u) &:= \int_{\mathbb{R}^d} (\nabla^T u)(y) (\nabla v_{\rho,x})(y) dy \\ &= \rho^{-d} \rho^{-1} \int_{\mathbb{R}^d} (\nabla^T u)(y) (\nabla v) \left( \frac{y-x}{\rho} \right) dy. \end{aligned}$$

Then

$$\begin{aligned} \lambda_{v_{\rho,x}}(u(h\cdot)) &= \rho^{-d-1} \int_{\mathbb{R}^d} (\nabla^T u(h\cdot))(y) (\nabla v) \left( \frac{y-x}{\rho} \right) dy \\ &= h \rho^{-d-1} \int_{\mathbb{R}^d} (\nabla^T u)(hy) (\nabla v) \left( \frac{hy-hx}{h\rho} \right) dy \\ &= h^{-d+1} \rho^{-d-1} \int_{\mathbb{R}^d} (\nabla^T u)(z) (\nabla v) \left( \frac{z-hx}{h\rho} \right) dz. \end{aligned}$$

On the other hand,

$$\begin{aligned} \lambda_{v_{h\rho,hx}}(u) &= (h\rho)^{-d-1} \int_{\mathbb{R}^d} (\nabla^T u)(z) (\nabla v) \left( \frac{z-hx}{h\rho} \right) dz \\ &= h^{-2} \lambda_{v_{\rho,x}}(u(h\cdot)). \end{aligned}$$

This results to scaling rule

$$\lambda_{v_{\rho,x}}(u(h\cdot)) = h^2 \lambda_{v_{h\rho,hx}}(u). \quad (6.6)$$

As another example, assume that  $v$  is the characteristic function of set  $B(0, 1)$ . Then the first inner product in (3.2) is vanished and the second one leads to the following functional

$$\lambda_{v_{\rho,x}}(u) = \rho^{-d} \int_{\partial B(x,\rho)} \nabla^T u(y) n(y) dy = \rho^{-d} \int_{\partial B(x,\rho)} \nabla^T u(y) \frac{y-x}{\rho} dy.$$

Scaling by  $h$  then gives

$$\begin{aligned} \lambda_{v_{\rho,x}}(u(h\cdot)) &= \rho^{-d} \int_{\partial B(x,\rho)} (\nabla^T u(h\cdot))(y) \frac{y-x}{\rho} dy \\ &= h\rho^{-d} \int_{\partial B(x,\rho)} (\nabla^T u)(hy) \frac{hy-hx}{h\rho} dy \\ &= h^{-d+2} \rho^{-d} \int_{\partial B(hx,h\rho)} (\nabla^T u)(z) \frac{z-hx}{h\rho} dz. \end{aligned}$$

On the other hand

$$\begin{aligned} \lambda_{v_{h\rho,hx}}(u) &= (h\rho)^{-d} \int_{\partial B(hx,h\rho)} \nabla^T u(y) \frac{y-hx}{h\rho} dy \\ &= h^{-2} \lambda_{v_{\rho,x}}(u(h\cdot)), \end{aligned}$$

which again yields the scaling rule (6.6). This rule is slightly different form (6.5) for  $s = 2$  because the functional on the right hand side of (6.6) is the scaled version of that on the left hand side. In the strong situation, one has a delta functional, and the scaling of the test function disappears. Here, the scaling in  $u$  implies a scaling in  $v$ , and vice versa. However, going to the details shows that the theory given in [4] is applicable for (6.6) with  $s = 2$ .

The scaling rule (6.6) is also very important in computational point of view where for a scalable approximation the stencil weights are only required to obtain for a fixed scale number and then divide by  $h^2$ .

On the other hand, although the authors of [3] consider the derivative functional  $\lambda = \delta_x \circ D^\alpha$ , their analysis can be easily extended to our local functionals as well.

In the following we assume that  $\Phi(x, y) := \phi(r)$  where  $r = \|x - y\|_2$ . Also the native space of  $\Phi$  is denoted by  $\mathcal{N}_\Phi$  with corresponding norm  $\|\cdot\|_{\mathcal{N}_\Phi}$ . We will use the notation

$$\partial^{\alpha,\beta} \Phi(x, y) := \frac{\partial^{|\alpha|}}{\partial x^\alpha} \left( \frac{\partial^{|\beta|}}{\partial y^\beta} \Phi(x, y) \right)$$

for brevity. By  $S_{x,Z}$  we mean  $\cup_{j=1}^n [x, z_j]$  where  $Z = \{z_1, \dots, z_n\}$  and  $[x, z]$  denotes for all real numbers lying on the line between  $x$  and  $z$ .

If  $s_{u,Z}$  is the  $\Phi$ -interpolant of  $u$  on set  $Z$  then it can be shown that  $\tilde{\lambda}u = \lambda s_{u,Z}$ , allowing us to use either one as necessary. Now, we have the following theorem form [3] which gives the error bound on each local stencil.

**Theorem 6.2** *Let  $\Phi$  be a conditionally positive definite kernel of order  $q$  on  $\Omega \subset \mathbb{R}^d$ , and let  $\lambda$  be a linear functional of scaling order  $s$  which is continuous on  $\mathcal{N}_\Phi$ . Further, assume that  $Z = \{z_1, \dots, z_n\} \subseteq \Omega$  is a  $\mathbb{P}_{q-1}^d$ -unisolvent set. Then for any  $x \in \Omega$  such that  $S_{x,Z} \subseteq \Omega$  and any  $\ell \geq \max\{q, s+1\}$  such that  $\partial^{\alpha,\beta} \Phi \in C(\Omega \times \Omega)$  for all  $|\alpha|, |\beta| \leq \ell$  we have*

$$|\lambda u(x) - \lambda s_{u,Z}(x)| \leq \varrho_{\ell,\lambda}(x, Z) \frac{\sqrt{M_{\Phi,\ell}}}{\ell!} \|u\|_{\mathcal{N}_\Phi}$$

for all  $u \in \mathcal{N}_\Phi$ , where

$$\varrho_{\ell,\lambda}(x, Z) = \sup \{ \lambda p(x) : p \in \mathbb{P}_\ell^d, |p(z_j)| \leq \|x - z_j\|_2^\ell, j = 1, \dots, n \}$$

is the growth function and

$$M_{\Phi,\ell}^2 = \sum_{|\alpha|, |\beta| \leq \ell} \binom{\ell}{\alpha} \binom{\ell}{\beta} \|\partial^{\alpha,\beta} \Phi\|_{C(\Omega \times \Omega)}.$$

Assume that  $z_j^h := x + h z_j$  and  $hZ = \{z_1^h, \dots, z_n^h\}$  for any  $h > 0$ . Then along the line of [3] we can show the growth function satisfies

$$\varrho_{\ell,\lambda}(x, hZ) = h^{\ell-s} \varrho_{\ell,\lambda}(x, Z),$$

where  $s$  is the scaling order of  $\lambda$ . Therefore we obtain from Theorem 6.2 for the scaled centers  $hZ$

$$|\lambda u(x) - \lambda s_{u,hZ}(x)| \leq h^{\ell-s} \varrho_{\ell,\lambda}(x, Z) \frac{\sqrt{M_{\Phi,\ell}}}{\ell!} \|u\|_{\mathcal{N}_\Phi}. \quad (6.7)$$

The stencil weights generated by  $hZ$  will not be in general the scaled version of the weights generated by  $Z$ . However, the error bound (6.7) works for both scalable and non-scalable stencils because we only use the scalability of  $\lambda$  on the right hand side.

We importantly note that in the above error bounds, if  $\Phi$  is smooth enough, integer  $\ell = \ell_{max}$  is the maximal possible order of polynomial unisolvency that set  $Z$  (or equivalently  $hZ$ ) allows. The stencil may not reproduce any polynomial at all. In addition, the assumptions on  $\Phi$  guarantee an enough smoothness to get the maximum rate  $\ell_{max} - s$  without any limitation from function  $u \in \mathcal{N}_\Phi$ . To make it more precise, we point that Davydov and Schaback [4] prove that the approximation of pointwise functionals of order  $s$  of functions in Sobolev space

$$H^m(\mathbb{R}^d) := \{f \in L_2(\mathbb{R}^d) : D^\alpha f \in L_2(\mathbb{R}^d), \forall \alpha \in \mathbb{N}_0^d \text{ with } |\alpha| \leq m\}$$

by linear combination of function values can not have a convergence rate better than  $m - s - d/2$ , no matter how many nodes are used and how large  $\ell$  is. They prove that this rate can be attained by any scalable approximation that are exact on polynomials of

order at least  $\lfloor m - d/2 \rfloor + 1$ . The unique stencil constructed by  $k = 2m - d > 0$  PHS kernel

$$H_{m,d}(r) := \begin{cases} r^{2m-d} \log r, & 2m - d \text{ even} \\ r^{2m-d}, & 2m - d \text{ odd} \end{cases} \quad (6.8)$$

by adding polynomials of some order  $\ell \geq \lfloor m - d/2 \rfloor + 1$  has optimal convergence rate  $m - s - d/2 = k/2 - s$  in Beppo-Levi space

$$\text{BL}_m(\mathbb{R}^d) := \{f \in C(\mathbb{R}^d) : D^\alpha f \in L_2(\mathbb{R}^d), \forall \alpha \in \mathbb{N}_0^d \text{ with } |\alpha| = m\}.$$

The above results of [4] show that this optimal rate will be also realized in Sobolev space  $H^m(\mathbb{R}^d)$ . We note here that  $H_{m,d}$  are conditionally positive definite of order  $\lfloor m - d/2 \rfloor + 1$  and have the Beppo-Levi spaces  $\text{BL}_m(\mathbb{R}^d)$  as their native spaces. More details can be found in [40, Chapters 8 and 10]. If  $\ell < m - d/2$  then the convergence rate in  $H^m(\mathbb{R}^d)$  cannot be better than  $\ell - s$ . We refer the reader to [4] for proofs and some more details including the crucial case  $\ell = m - d/2$ .

Since the approximation via PHS is scalable, one can form the stencil for a fixed set  $Z$  around the origin and then rescale the obtained weights for set  $hZ$  by dividing by  $h^s$ . This allows avoiding the ill-conditioning of the interpolation matrix for small values of  $h$ . This simple idea was first reported in [15] for a pure interpolation problem with  $s = 0$ . For nonscalable stencils other tricks which are described in section 5 might be used. For example the RBF-QR or the RBF-GA algorithms can be used when  $\Phi$  is a Gaussian kernel.

Authors of [4] prove further that the renormalized weights of an optimal nonscalable approximation in Sobolev space converge to the weights of a scalable approximation as  $h$  goes to zero. Thus, if  $\Phi$  has  $H^m(\mathbb{R}^d)$  as its native space then the unique stencil constructed by  $\Phi$  (with or without polynomial reproduction, scalable or nonscalable) is nearly optimal in Sobolev space  $H^m(\mathbb{R}^d)$  with approximate rate  $\min\{m - s - d/2, \ell_{max} - s\}$  for small values of  $h$ . For infinitely smooth kernels such as Gaussian, the convergence rates will be  $\ell_{max} - s$  for smooth functions in their native spaces. However, if that error is measured for finitely smooth functions in  $H^m(\mathbb{R}^d)$  then the convergence rate cannot be better than  $m - s - d/2$ , as it is pointed before.

## 6.2 Stability

We turn to the stability issue by measuring the stability constant  $C_S(A)$ . Despite the lack of a theoretical bound, Schaback [31] has proposed some numerical estimators for this constant. For example, in case  $p = q = 2$ ,

$$C_S(A) = \left( \min_{1 \leq j \leq N} \sigma_j \right)^{-1}$$

for the  $N$  positive singular values  $\sigma_1, \dots, \sigma_N$  of  $A$ , and these are obtainable by singular value decomposition (SVD). Also, the  $(q, p)$ -norm of the pseudoinverse of  $A$ , defined by

$$\|A^\dagger\|_{q,p} := \sup_{\mathbf{v} \neq 0} \frac{\|A^\dagger \mathbf{v}\|_q}{\|\mathbf{v}\|_p},$$

overestimates  $C_S(A)$ . Finally, a simple possibility, restricted to square systems, is to use the fact that MATLAB's `condest` command estimates the  $L_1$  condition number, which is the  $L_\infty$  condition number of the transpose. Thus

$$\tilde{C}_S(A) := \frac{\text{condest}(A')}{\|A\|_\infty}$$

is an estimate of the  $L_\infty$  norm of  $A^{-1}$ . This is computationally very cheap for sparse matrices and turns out to work fine on the examples in section 7, but an extension to non-square matrices is missing.

The above postprocessing estimators may give some insight into how the method works in the numerical stability point of view.

### 6.3 Eigenvalue stability

For time dependent PDEs, a necessary condition for stability of the Method of Lines (MOL) is that the eigenvalues of the discretization matrices must be in the stability domain of the ODE solver used for advancing the system in time. For instance, the forward time difference scheme for the well-known parabolic equation  $u_t = Lu$  in  $\Omega \subset \mathbb{R}^d$  with boundary condition  $u = 0$  on  $\Gamma$  and a prescribed nonzero initial condition is

$$\begin{aligned} \mathbf{u}_\Omega^{(n+1)} &= (I + \Delta t A) \mathbf{u}_\Omega^{(n)} \\ \mathbf{u}_\Gamma^{(n+1)} &= 0 \end{aligned}$$

for  $n = 0, 1, \dots, N_T$  and  $\Delta t = t_{\text{final}}/N_T$ . Here  $\mathbf{u}_\Omega$  and  $\mathbf{u}_\Gamma$  are vectors of interior and boundary nodal values, respectively, and  $\mathbf{u}^{(n)} = \mathbf{u}(n\Delta t)$ .  $A$  is the differentiation matrix of operator  $L$ . If  $\lambda = \lambda(A)$  stands for an eigenvalue<sup>1</sup> of  $A$ , a time stability condition is  $|1 + \Delta t \lambda| < 1$  which is equivalent to

$$\text{Re}(\lambda) < 0, \tag{6.9}$$

$$\Delta t < 2 \frac{|\text{Re}(\lambda)|}{|\lambda|^2}. \tag{6.10}$$

Unfortunately, there exists no theoretical proof for (6.9) for RBF-FD discretizations. For strong-based methods, experimental results of [2, 14, 26] and others show that it is satisfied

---

<sup>1</sup>Despite the notation in the whole paper that  $\lambda$  (with or without subscripts) is used for functionals, here  $\lambda$  stands for eigenvalues.

for some kinds of kernels and point distributions. In other cases, eigenvalues with positive real parts can cause spurious growth in the numerical solutions of advection-diffusion equations [5, 6, 8, 33]. This problem might be resolved by adding small vanishing amount of artificial *hyperviscosity*  $(-1)^{p-1}\gamma_h\Delta^p u$  to the model to gain  $u_t = Lu + (-1)^{p-1}\gamma_h\Delta^p u$ . Here  $\gamma_h$  is a small positive number going rapidly to zero as  $h$  (the fill distance) decreases. In the weak-based method, the hyperviscosity term can be easily applied after a recursively use of the Gauss divergence theorem to obtain

$$\int_B \Delta^p u v \, dx = \int_B \Delta^{\lceil p/2 \rceil} u \Delta^{\lfloor p/2 \rfloor} v \, dx, \quad v \in H_0^{2\lfloor p/2 \rfloor}(B), \quad (6.11)$$

where

$$H_0^p(B) := \left\{ v \in H^p(B) : \Delta^k v = \frac{\partial \Delta^k v}{\partial n} = 0 \text{ on } \partial B, \text{ for } k = 0, 1, \dots, \frac{p}{2} - 1 \right\}.$$

In our local bilinear forms on  $B = B(x_k, \rho)$ , any smooth, compactly supported on  $B$  and radial basis function satisfies the boundary conditions in the definition of  $H_0^p(B)$ . For example, the Wendland's function  $\phi_{3,2}(r) := (1-r)_+^6(35r^2 + 18r + 3)$  lies on  $H_0^5(B(0,1))$  for  $r = \|x\|$ ,  $x \in \mathbb{R}^2$ , allowing to use  $v = \phi_{3,2}(\|\cdot\|_2)$  to weaken the hyperviscosity terms  $\Delta^p u$  for  $p = 1, 2, 3, 4, 5$  as in (6.11)<sup>2</sup>. Of course, reducing to a half-order derivative is an advantage of the new method when a hyperviscosity term needs to be added. We do not pursue this further and leave it for a future paper on advection-diffusion problems, instead we will give some experimental results in section 7.

## 7 Applications

In this section, first the method is tested on the well-known elliptic problem of Poisson equation and then an application is given for a two dimensional elasticity problem.

### 7.1 Poisson equation

Let  $\Omega = (0,1)^2$ . We are going to examine the proposed numerical scheme for PDEs with true solutions that lie on Sobolev spaces. Since such solutions are not explicitly at hand, a manipulated solution is constructed below using the smoothness properties of *Sobolev kernel*. Assume  $\{\xi_1, \dots, \xi_n\}$  is a set of points in  $\Omega$  and define

$$u(x) := \sum_{k=1}^n c_k \psi_\beta(\varepsilon \|x - \xi_k\|_2), \quad x \in \Omega, \quad \varepsilon = 5, \quad (7.1)$$

for some known coefficients  $c_k$ , where  $\psi_\beta(r) = r^{\beta-1}K_{\beta-1}(\varepsilon r)$ ,  $\beta > 1$  is the Sobolev spline of Table 1 with  $d = 2$ . Since the Fourier Transform of  $\Psi = \psi(\|\cdot\|_2)$  behaves like  $(1 + \|\cdot\|_2^2)^{-\beta}$

---

<sup>2</sup>Wendland's function  $\phi_{3,2}(\|\cdot\|_2)$  lies actually on  $H^\tau(\mathbb{R}^2)$  for all  $\tau < 6$ .

we can prove that  $\Psi$  belongs to  $H^t(\Omega)$  for all  $t < 2\beta - 1$ , so does  $u$ . We can play with  $\beta$  to construct various finitely smooth solutions. The right hand side functions  $f$  and  $g$  in (2.1)-(2.2) with  $L = \Delta$  and  $B = Id$  are calculated, accordingly. In experiments we use  $\{\xi_1, \dots, \xi_{121}\}$  random points in  $\Omega$  and

$$\tilde{\mathbf{c}} = (0.1, -0.2, 0.4, 0.3, -0.1, -0.4, 0.3, -0.5, 0.1, 0.7, -0.4), \quad \mathbf{c} = \underbrace{(\tilde{\mathbf{c}}, -\tilde{\mathbf{c}}, \dots, \tilde{\mathbf{c}}, -\tilde{\mathbf{c}})}_{11 \text{ times}}.$$

The surface and contour plots of this function for  $\beta = 1.5$  and  $\beta = 2$  are shown in Figure 1. Note that, we just use the Sobolev kernel to construct a true solution for the PDE to test the proposed method. Other kernels (Gaussian and PHS) are used for the approximation process.

To compute the stencil weights stably and efficiently, the RBF-QR algorithm is used for Gaussian and the scaling rule (6.6) is employed for PHS. Besides, the experimental results are obtained via:

- a sequence of regular or Halton point sets  $X$  with fill distance  $h$  on  $[0, 1]^2$  (see Figure 2 for  $N = 841$  and  $h \approx 0.036$ ),
- shape parameter  $\varepsilon = 0.1$  for Gaussian RBF,
- RBF parameters  $k = 2, 3, 4, 5, 6, 8$  for PHS,
- the radius of local subdomains  $\rho = c_1 h$  where  $c_1 = 0.25$ ,
- the radius of stencils  $\delta = c_2 h$  where  $c_2 \geq 4$  is chosen (per any test point) enough large to have at least 21 points in each Gaussian stencil and  $(\ell + 2)(\ell + 1)/2$  points in PHS stencils where  $\ell = \lfloor k/2 \rfloor + 1$ ,
- a 15-point Gauss-Legendre quadrature and its corresponding tensor product rule for computing the boundary and domain integrals in local bilinear forms  $\lambda_k = a_{\rho,k}(\cdot, v)$  and local linear forms  $b_k = \ell_{\rho,k}(v)$ .

From here on, Gaussian is abbreviated to GA, PHS with parameter  $k$  to PHS $k$ , Halton points to Hpoints and regular points to Rpoints.

First, we run the strong-based and the weak-based algorithms for four cases  $\beta = 1.5$  ( $u \in H^{2-}(\Omega)$ ),  $\beta = 2$  ( $u \in H^{3-}(\Omega)$ ),  $\beta = 3$  ( $u \in H^{5-}(\Omega)$ ) and  $\beta = 4$  ( $u \in H^{7-}(\Omega)$ ) for comparison. By  $u \in H^{\tau-}$  we mean  $u \in H^t$  for any  $t < \tau$ . Results of the absolute errors in discrete norm infinity (on a fine point set with fill distance  $h = 1/30$ ) are plotted for GA, PHS2 and PHS5 in Figures 3, 4 and 5, respectively. Information about parameters and discussions are appeared in titles and captions of figures. Since PHS2 has a low smoothness as a basis function, the results of the weak-based method are superior, regardless the smoothness of true solutions. In other cases (GA and PHS5), where no limitation is

caused by the smoothness of the basis function itself, for less smooth solutions the new method works much better while for smooth solutions both methods have approximately the same rates of convergence. The above results are obtained for scattered Hpoints. In Figure 6 the results on Rpoints with GA kernel are presented. Comparing with that on Hpoints, we observe some (slightly) more accurate results for smooth solutions. We omit the corresponding figures for PHS2 and PHS5 on Rpoints.

The absolute errors in discrete norm infinity (on trial points) of the weak-based RBF-FD method and the classical five-point FD method are compared in Figure 7. We have to use only Rpoints in this experiment because the classical FD method does not work on arbitrary scattered points. Since the native space of PHS $k$ ,  $k$  even, is  $\text{BL}_{k/2+1}(\mathbb{R}^2)$ , the true solution  $u \in H^{5-}(\Omega)$  is chosen for  $k = 2, 4, 6, 8$ . For these choices of  $k$  the native space  $\text{BL}_{k/2+1}(\mathbb{R}^2)$  is a subset of  $H^{5-}(\mathbb{R}^2)$ . As is shown in Figure 7, classical FD is more accurate than RBF-FD with PHS2 while it is less accurate than RBF-FD with other PHS kernels. The average computational order of convergence of the classical FD is 1.85 while it is 0.13, 1.56, 2.00 and 2.68 for PHS $k$  for  $k = 2, 4, 6$  and 8, respectively. Remember that polynomials of orders  $q = 2, 3, 4, 5$  need to be added to the PHS $k$  expansion for  $k = 2, 4, 6, 8$ , respectively.

The effect of shape parameter  $\varepsilon$  of GA on accuracy is shown in Figure 8 where the absolute norm infinity of errors are plotted in terms of  $\varepsilon$  values for true solution  $u \in H^{7-}(\Omega)$ . Smaller values of  $\varepsilon$  (values between  $10^{-3}$  and 1.0) produce approximately the same results while bigger values fail to give a desirable accuracy. All other GA numerical experiments of this paper are obtained with  $\varepsilon = 0.1$ .

To analyze the effect of the smoothness of true solutions, in Figure 9 the results of the weak-based method for various  $\beta$  values are compared on Rpoints with GA kernel. In this case, stencils contain, at least, 21 points which is corresponded to polynomial consistency of order  $\ell = 6$  in  $\mathbb{R}^2$ . As we see, for less smooth solutions the rate of convergence is controlled by the smoothness of  $u$  which is increased as  $\beta$  increases until touching the maximum polynomial consistency order  $\ell$ . Thereafter, the higher smoothness dose not essentially improve the convergence rate; it remain at  $\ell - s = \ell - 2 \approx 4$ .

In Figure 10 the stability constants  $C_S$  and  $\tilde{C}_S$  of the new method are plotted in terms of  $h$ . These constants measure the conditioning of the final linear system (4.4) which is different from the conditioning of local problems (4.2) or (4.3) which were improved by either the RBF-QR algorithm for GA or the scaling property for PHS. As expected, the method possesses an excellent stability as well as any sparse FD scheme. The (approximately) same stability results are obtained for the strong-based method which are not given here.

Figures 11, 12 and 13 show the spectrum of the discrete Laplacian for PHS2, PHS6 and GA kernels, respectively, on 841 Rpoints (left profiles) and Hpoints (right profiles). In all cases, except that of GA on Hpoints, eigenvalues all fall in the left half plane. While not presented here, similar behaviours were obtained for other PHS kernels and various

values of  $N$ .

As shown in Figure 13 (right side), in the case of GA on Hpoints, few eigenvalues have positive real parts. As discussed in section 6.3, the hyperviscosity stabilization procedure can be used for shifting the eigenvalues to the left half plane without a reduction in accuracy. Results are rather sensitive to the choice of both hyperviscosity order  $p$  and hyperviscosity amount  $\gamma_h$ . Some criteria are given in [33] for strong-based methods. Here we apply the hyperviscosity term  $\Delta^5 u$ , weaken it according to (6.11) and discretize it by PHS9 kernel. Values  $\gamma_h = \mathcal{O}(h^{12})$  seem to give convincing results in this case. The spectrum of the differentiation matrix on 841 Hpoints is given in Figure 14. As we see, all eigenvalues now lie on the left half plane. However, a more deep investigation on hyperviscosity stabilization of weak-based method is required that we leave it for a future study.

## 7.2 Elasticity problem

Let  $\Omega \subset \mathbb{R}^2$  is a bounded domain with boundary  $\Gamma$ . In a tensorial notation, we consider the following two dimensional elasto-static problem

$$\sigma_{ij,j} + f_i = 0, \quad \text{in } \Omega, \quad (7.2)$$

where  $[\sigma_{11}, \sigma_{22}, \sigma_{12}]^T =: \sigma$  is the stress tensor, which corresponds to the displacement field  $[u_1, u_2]^T =: u$ , and  $[f_1, f_2]^T =: f$  is the body force. In the above formulation  $\sigma = DLu$  where the derivative matrix  $L$  is defined as

$$L = \begin{bmatrix} \frac{\partial}{\partial x^1} & 0 \\ 0 & \frac{\partial}{\partial x^2} \\ \frac{\partial}{\partial x^2} & \frac{\partial}{\partial x^1} \end{bmatrix}$$

and for a problem of isotropic material, the stress-strain matrix  $D$  is defined by

$$D = \frac{\bar{E}}{1 - \bar{\nu}^2} \begin{bmatrix} 1 & \bar{\nu} & 0 \\ \bar{\nu} & 1 & 0 \\ 0 & 0 & (1 - \bar{\nu})/2 \end{bmatrix},$$

where

$$\bar{E} = \begin{cases} E & \text{for plane stress} \\ \frac{E}{1 - \nu^2} & \text{for plane strain} \end{cases} \quad \bar{\nu} = \begin{cases} \nu & \text{for plane stress} \\ \frac{\nu}{1 - \nu} & \text{for plane strain} \end{cases},$$

in which  $E$  and  $\nu$  are Young's modulus and Poisson's ratio, respectively. The corresponding boundary conditions for (7.2) are given by

$$\begin{aligned} u_i &= \bar{u}_i, & \text{on } \Gamma_u, \\ t_i &= \sigma_{ij} n_j = \bar{t}_i, & \text{on } \Gamma_t, \end{aligned}$$

where  $[\bar{u}_1, \bar{u}_2]^T =: \bar{u}$  and  $[\bar{t}_1, \bar{t}_2]^T =: \bar{t}$  are the prescribed displacement and traction, respectively, and  $[n_1, n_2]^T =: n$  is the unit outward normal to the boundary  $\Gamma = \Gamma_u \cup \Gamma_t$ .

Taking integration with respect to the spatial variable from both sides of equation (7.2) against a proper test function  $v$  and then applying the Gauss divergence theorem, the local weak forms

$$\int_{\partial B(x_k, \rho)} v \mathcal{N} D L u \, dx - \int_{B(x_k, \rho)} \varepsilon_v D L u \, dx = \int_{B(x_k, \rho)} f v \, dx, \quad \rho > 0 \quad (7.3)$$

are derived for  $k = 1, 2, \dots, n_X$  where  $n_X$  is the number of points inside  $\Omega$ , and

$$\mathcal{N} = \begin{bmatrix} n_1 & 0 & n_2 \\ 0 & n_2 & n_1 \end{bmatrix}, \quad \varepsilon_v = \begin{bmatrix} v_{,1} & 0 & v_{,2} \\ 0 & v_{,2} & v_{,1} \end{bmatrix}.$$

The boundary conditions may be imposed using a proper collocation method by defining the identity functional

$$\lambda_k u := u(y_k) \quad y_k \in \Gamma_u$$

for essential boundary conditions and

$$\lambda_k u := (\mathcal{N} D L u)(y_k), \quad y_k \in \Gamma_t$$

for traction boundary conditions. On the other side, we define for internal points  $x_k$ ,

$$\lambda_k u := - \int_{B(x_k, \rho)} \varepsilon_v D L u \, dx + \int_{\partial B(x_k, \rho)} v \mathcal{N} D L u \, dx.$$

The right hand side is defined accordingly by

$$b_k = \begin{cases} \bar{u}(y_k), & y_k \in \Gamma_u \\ \bar{t}(y_k), & y_k \in \Gamma_t \\ \int_{B(x_k, \rho)} f v \, dx, & x_k \in \text{int}(\Omega) \end{cases}$$

to finally get the following abstract functional forms

$$\lambda_k u = b_k, \quad k = 1, 2, \dots, N.$$

The problem takes the appropriate form for applying the RBF-FD method. We omit the implementation details and just give the results of a benchmark problem in 2D elasticity.

Consider an infinite plate with a central hole  $(x^1)^2 + (x^2)^2 \leq a^2$  of radius  $a$ , subjected to a unidirectional tensile load of  $\sigma_0 = 1$  in the  $x^1$ -direction at infinity [35]. There is an analytical solution for stress in the polar coordinate  $(r, \theta)$

$$\begin{aligned} \sigma_{11} &= \sigma_0 \left[ 1 - \frac{a^2}{r^2} \left( \frac{3}{2} \cos 2\theta + \cos 4\theta \right) + \frac{3a^4}{2r^4} \cos 4\theta \right], \\ \sigma_{12} &= \sigma_0 \left[ -\frac{a^2}{r^2} \left( \frac{1}{2} \sin 2\theta + \sin 4\theta \right) + \frac{3a^4}{2r^4} \sin 4\theta \right], \\ \sigma_{22} &= \sigma_0 \left[ -\frac{a^2}{r^2} \left( \frac{1}{2} \cos 2\theta - \cos 4\theta \right) - \frac{3a^4}{2r^4} \cos 4\theta \right], \end{aligned}$$

with the corresponding displacements

$$u_1 = \frac{1 + \bar{\nu}}{E} \sigma_0 \left[ \frac{1}{1 + \bar{\nu}} r \cos \theta + \frac{2}{1 + \bar{\nu}} \frac{a^2}{r} \cos \theta + \frac{1}{2} \frac{a^2}{r} \cos 3\theta - \frac{1}{2} \frac{a^4}{r^3} \cos 3\theta \right],$$

$$u_2 = \frac{1 + \bar{\nu}}{E} \sigma_0 \left[ \frac{-\bar{\nu}}{1 + \bar{\nu}} r \sin \theta - \frac{1 - \bar{\nu}}{1 + \bar{\nu}} \frac{a^2}{r} \sin \theta + \frac{1}{2} \frac{a^2}{r} \sin 3\theta - \frac{1}{2} \frac{a^4}{r^3} \sin 3\theta \right].$$

In computations we consider a finite plate, a disk of radius  $b = 4$  with a circular hole of radius  $a = 1$ , where the solution is very close to that of the infinite plate [35]. Due to symmetry, only the upper right quadrant of the plate, as is shown with a set of 990 points in Figure 15, is modelled. The traction boundary conditions given by the exact solution are imposed on the outer circular boundary. Symmetry conditions are imposed on the left and bottom edges, i.e.,  $u_1 = 0$ ,  $t_2 = 0$  are prescribed on the left edge and  $u_2 = 0$ ,  $t_1 = 0$  on the bottom edge, and the inner boundary at  $a = 1$  is traction free, i.e.  $t_1 = t_2 = 0$ .

Numerical results are presented for a plane stress case with  $E = 1.0$  and  $\nu = 0.25$ . The GA basis function and a sequence of sets points  $X$  of sizes  $N = 81, 272, 990, 3770$  with fill distances  $h \approx 0.2, 0.1, 0.05, 0.025$ , where the third set is depicted in Figure 15, are used in this example. We use a finer discretization near the inner circle because the most action of the problem takes place there. This will send the distribution of points out of the quasi-uniformity. However, our localized meshless method still works properly. The same integration rule as that is used in the previous example is employed here. Results of the relative discrete 2-norm errors (at a very fine set points) of the displacement field and normal/shear stresses are shown in Figure 16. Since both displacement field and its derivatives are smooth, the rates are determined by the maximum order of polynomial recovery that stencil points allow; here  $\ell - 2 = 4$ . Moreover, the exact normal stress  $\sigma_{11}$  at  $x^1 = 0$  is compared with the numerical solution (by using the set point in Figure 15) in Figure 17.

## 8 Conclusion

In this paper, a new weak-based RBF-generated finite difference method is proposed. The PDE and its boundary conditions are discretized to a set of testing functionals consisting of local weak forms. The stencil weights for approximating the local functionals are obtained by a local RBF approximation method. The convergence properties and the stability issues are considered and some useful features of the method are outlined. In particular, the method can be applied on problems with low smooth solutions. Also, lower derivatives of the RBF space are required. Some experimental results are given to illustrate the performance of the new method. Although we believe that the method can be applied to a large class of PDE problems in engineering and sciences, an application to time-dependent PDEs still needs more considerations. In subsection 6.3, an eigenvalue

analysis for the time stability is discussed and in section 7 some experimental results are given. However, theoretical or (at least) experimental investigations are still required to estimate the amount of hyperviscosity and to show the effect of the degree of polynomials in PHS kernels. These are left for a future study.

## Acknowledgments

Special thanks go to Prof. Robert Schaback (Universität Göttingen) for his helpful comments about the scaling argument of section 6. The second author was in part supported by a Grant from Institute for Research in Fundamental Sciences, IPM, No. 98650422.

## References

- [1] S.N. Atluri and T.-L. Zhu. A new meshless local Petrov-Galerkin (MLPG) approach in Computational mechanics. *Computational Mechanics*, 22:117–127, 1998.
- [2] G. A. Barnett. *A robust RBF-FD formulation based on polyharmonic splines and polynomials*. PhD thesis, University of Colorado, Boulder, 2015.
- [3] O. Davydov and R. Schaback. Error bounds for kernel based numerical differentiation. *Numerische Mathematik*, 132:243–269, 2016.
- [4] O. Davydov and R. Schaback. Optimal stencils in Sobolev spaces. *IMA Journal of Numerical Analysis*, In press, 2018.
- [5] N. Flyer, G. A. Barnett, and L. J. Wicker. Enhancing finite differences with radial basis functions: Experiments on the Navier-Stokes equations. *Journal of Computational Physics*, 316:39–62, 2016.
- [6] N. Flyer, E. Lehto, S. Blaise, G. B. Wright, and A. St-Cyr. A guide to RBF-generated finite differences for nonlinear transport: shallow water simulations on a sphere. *Journal of Computational Physics*, 231:4078–4095, 2012.
- [7] B. Fornberg and N. Flyer. Solving PDEs with radial basis functions. *Acta Numerica*, pages 215–258, 2015.
- [8] B. Fornberg, E. Larsson, and N. Flyer. Stable computations with Gaussian radial functions. *SIAM Journal on Scientific Computing*, 33:869–892, 2011.
- [9] B. Fornberg and E. Lehto. Stabilization of RBF-generated finite difference methods for convective PDEs. *Journal of Computational Physics*, 230:2270–2285, 2011.

- [10] B. Fornberg, E. Lehto, and C. Powell. Stable calculation of Gaussian-based RBF-FD stencils. *Computers and Mathematics with Applications*, 65:627–635, 2013.
- [11] B. Fornberg and C. Piret. A stable algorithm for flat radial basis functions on a sphere. *SIAM Journal on Scientific Computing*, 30:60–80, 2007.
- [12] B. Fornberg and G. B. Wright. Stable computation of multiquadric interpolants for all values of the shape parameter. *Computers & Mathematics with Applications*, 48:853–867, 2004.
- [13] C. Franke and R. Schaback. Convergence order estimates of meshless collocation methods using radial basis functions. *Advances in Computational Mathematics*, 8:381–399, 1998.
- [14] E. J. Fuselier and G. B. Wright. A high-order kernel method for diffusion and reaction-diffusion equations on surfaces. *Journal of Scientific Computing*, 56:535–565, 2013.
- [15] A. Iske. On the approximation order and numerical stability of local lagrange interpolation by polyharmonic splines. In *International Series of Numerical Mathematics 145*, pages 153–165, Basel, 2003. Birkhäuser Verlag.
- [16] E. J. Kansa. Multiquadrics —A scattered data approximation scheme with applications to computational fluid-dynamics, I. Surface approximations and partial derivative estimates. *Computers & Mathematics with Applications*, 19:127–145, 1990.
- [17] E. J. Kansa. Multiquadrics —A scattered data approximation scheme with applications to computational fluid-dynamics, II. Solutions to parabolic, hyperbolic and elliptic partial differential equations. *Computers & Mathematics with Applications*, 19:147–161, 1990.
- [18] E. Larsson, E. Lehto, A. Heryudono, and B. Fornberg. Stable computation of differentiation matrices and scattered node stencils based on Gaussian radial basis functions. *SIAM Journal on Scientific Computing*, 35:A2096–A2119, 2013.
- [19] Q. T. Le Gia. Galerkin approximation for elliptic PDEs on spheres. *Journal of Approximation Theory*, 130:123–147, 2004.
- [20] S. De Marchi and G. Santin. A new stable basis for radial basis function interpolation. *Journal of Computational and Applied Mathematics*, 253:1–13, 2013.
- [21] S. De Marchi and G. Santin. Fast computation of orthonormal basis for RBF spaces through Krylov space methods. *BIT Numerical Mathematics*, 5:949–966, 2015.

- [22] S. De Marchi and R. Schaback. Stability of kernel-based interpolation. *Advances in Computational Mathematics*, 32:155–161, 2010.
- [23] D. Mirzaei. Direct approximation on spheres using generalized moving least squares. *BIT Numerical Mathematics*, 57:1041–1063, 2017.
- [24] D. Mirzaei. A Petrov–Galerkin kernel approximation on the sphere. *SIAM Journal on Numerical Analysis*, 56:274–295, 2018.
- [25] D. Mirzaei, R. Schaback, and M. Dehghan. On generalized moving least squares and diffuse derivatives. *IMA Journal of Numerical Analysis*, 32:983–1000, 2012.
- [26] V. Mohammadi, D. Mirzaei, and M. Dehghan. Numerical simulation and error estimation of the time-dependent allen-cahn equation on surfaces with radial basis functions. *Journal of Scientific Computing*, In press, 2018.
- [27] S. Müller and R. Schaback. A Newton basis for kernel spaces. *Journal of Approximation Theory*, 161:645–655, 2009.
- [28] M. Pazouki and R. Schaback. Bases for kernel-based spaces. *Journal of Computational and Applied Mathematics*, 236:575–588, 2011.
- [29] R. Schaback. Convergence of unsymmetric kernel-based meshless collocation methods. *SIAM Journal on Numerical Analysis*, 45:333–351, 2007.
- [30] R. Schaback. Direct discretization with application to meshless methods for PDEs. In *Dolomites Research Notes on Approximation, Proceedings of DWCAA12*, volume 6, pages 37–51, 2013.
- [31] R. Schaback. Error analysis of nodal meshless methods. In *Meshfree Methods for Partial Differential Equations VIII, Lecture Notes in Computational Science and Engineering 115*, pages 117–143, Bonn, 2015. Springer 2017.
- [32] R. Schaback. All well-posed problems have uniformly stable and convergent discretizations. *Numerische Mathematik*, 132:597–630, 2016.
- [33] V. Shankar and A. L. Fogelson. Hyperviscosity-based stabilization for radial basis function-finite difference (RBF-FD) discretizations of advection-diffusion equations. *Journal of Computational Physics*, 372:616–639, 2018.
- [34] C. Shu, H. Ding, and K. S. Yeo. Local radial basis function-based differential quadrature method and its application to solve two-dimensional incompressible navier-stokes equations. *Computer Methods in Applied Mechanics and Engineering*, 192:941–954, 2003.

- [35] S. P. Timoshenko and J. N. Goodier. *Theory of Elasticity*. 3rd edition. McGraw-Hill, New York, 1970.
- [36] A. E. Tolstykh. On using RBF-based differencing formulas for unstructured and mixed structured-unstructured grid calculations. In *Proceedings of the 16th IMACS World Congress 228*, pages 4606–4624, Lausanne, 2000.
- [37] A. E. Tolstykh. On using radial basis functions in a “finite difference mode” with applications to elasticity problems. *Computational Mechanics*, 33:68–79, 2003.
- [38] H. Wendland. Piecewise polynomial, positive definite and compactly supported radial basis functions of minimal degree. *Advances in Computational Mathematics*, 4:389–396, 1995.
- [39] H. Wendland. Meshless Galerkin methods using radial basis functions. *Mathematics of Computation*, 68:1521–1531, 1999.
- [40] H. Wendland. *Scattered Data Approximation*. Cambridge University Press, 2005.
- [41] G. B. Wright. *Radial basis function interpolation: Numerical and analytical developments*. PhD thesis, University of Colorado, Boulder, 2003.
- [42] G. B. Wright and B. Fornberg. Stable computations with flat radial basis functions using vector-valued rational approximations. *Journal of Computational Physics*, 331:137–156, 2017.
- [43] Z. Wu. Hermite Birkhoff interpolation of scattered data by radial basis functions. *Approximation Theory and its Applications*, 8:1–10, 1992.

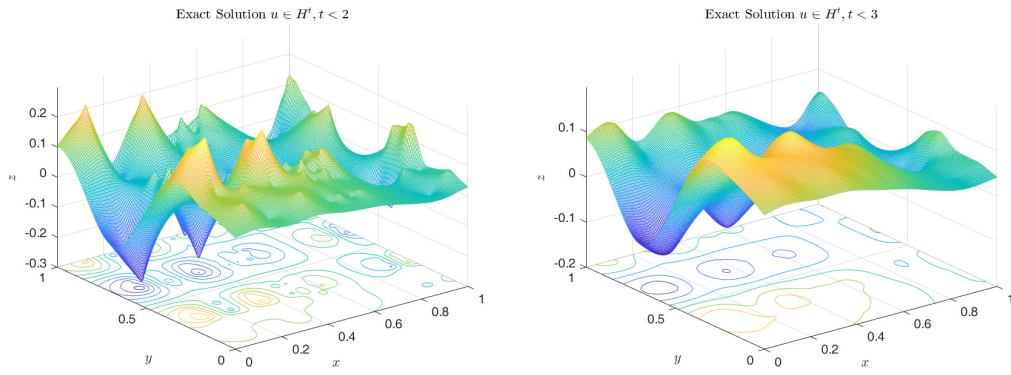


Figure 1: Exact solutions defined in (7.1) for two values  $\beta = 1.5$  (left) and  $\beta = 2$  (right).

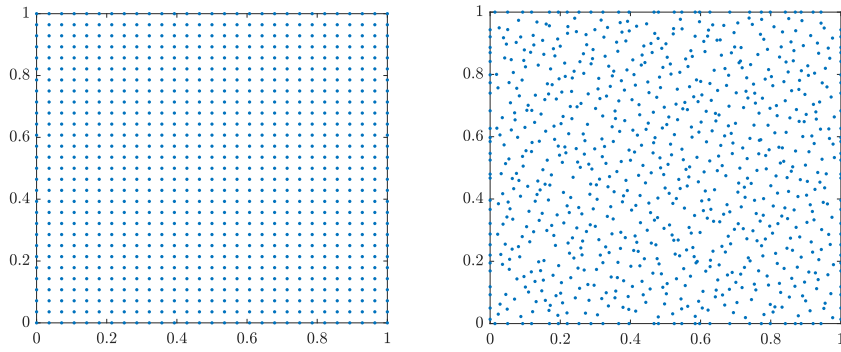


Figure 2: Regular (left) and Halton (right) points ( $N = 841$ ).

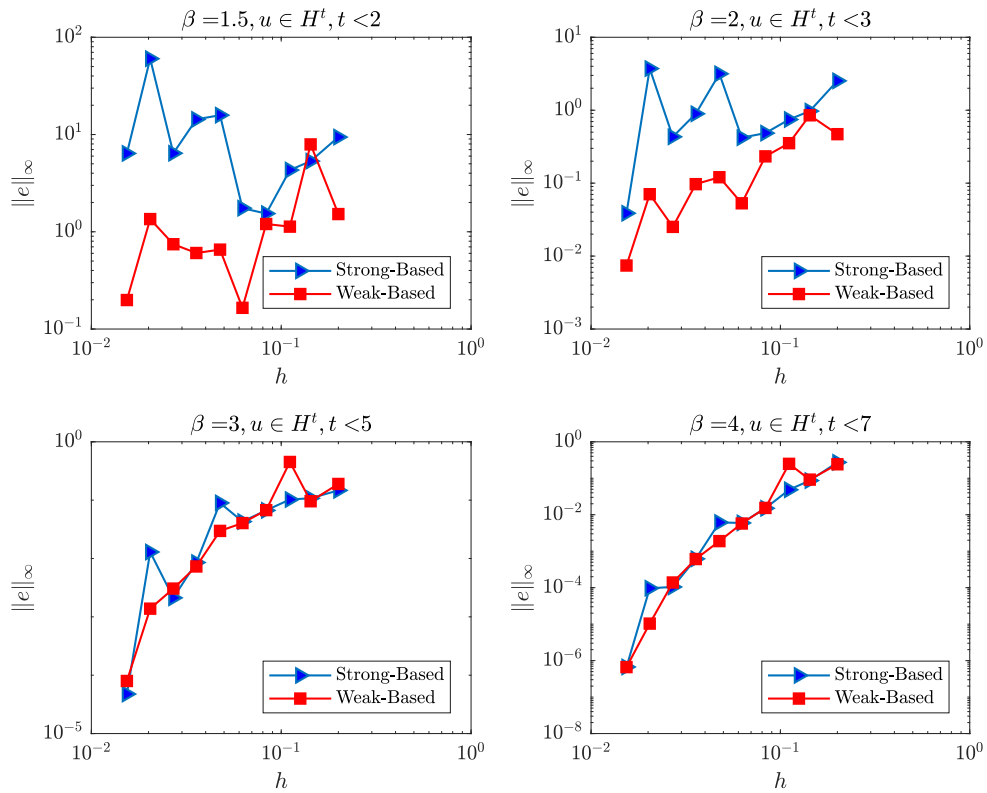


Figure 3: Comparing the absolute errors (discrete norm infinity) of the strong- and the weak-based methods for various true solutions of different smoothness; GA on Halton points.

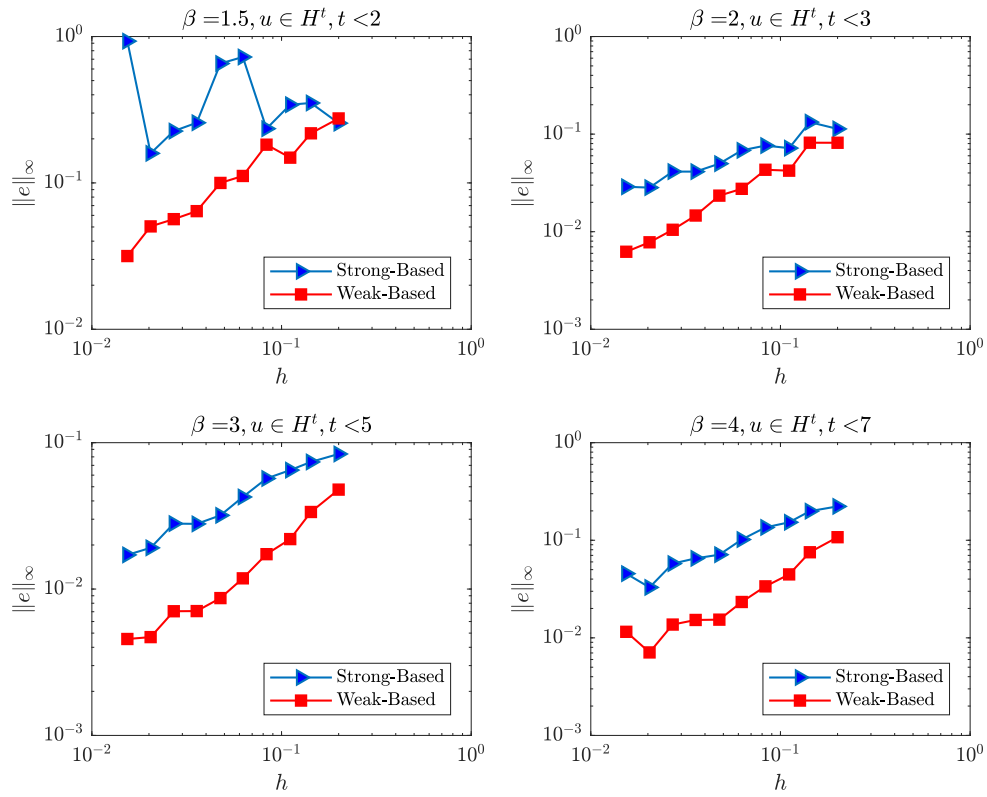


Figure 4: Comparing the absolute errors (discrete norm infinity) of the strong- and the weak-based methods for various true solutions of different smoothness; PHS2 on Halton points.

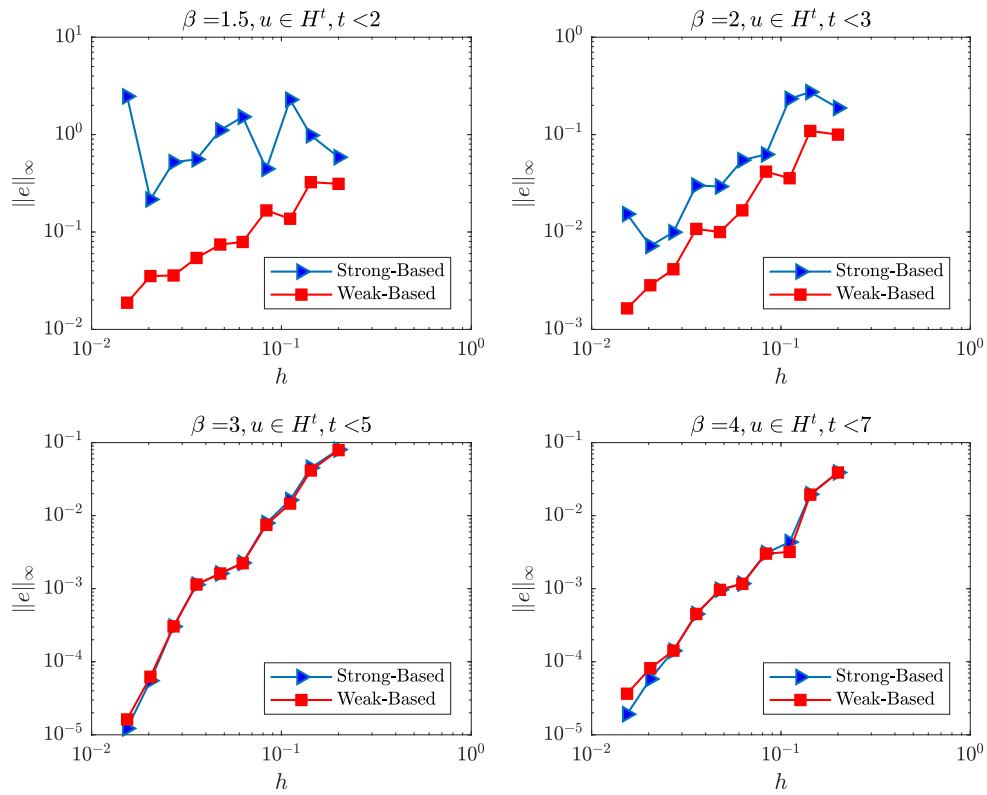


Figure 5: Comparing the absolute errors (discrete norm infinity) of the strong- and the weak-based methods for various true solutions of different smoothness; PHS5 on Halton points.

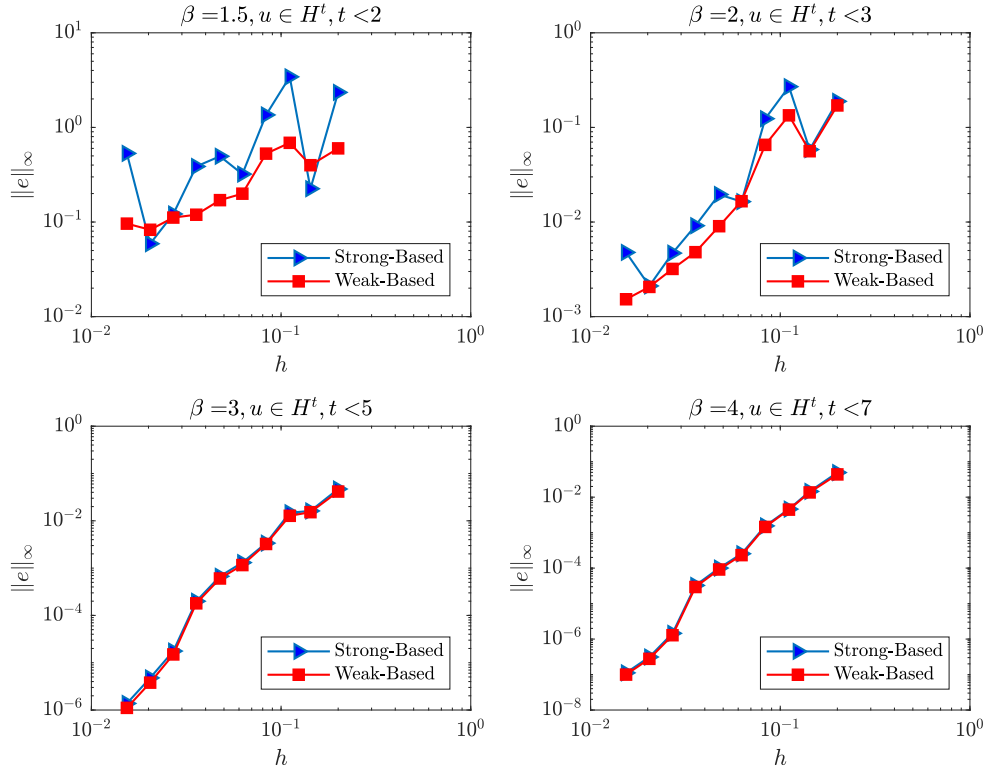


Figure 6: Comparing the absolute errors (discrete norm infinity) of the strong- and the weak-based methods for various true solutions of different smoothness; GA on regular points.

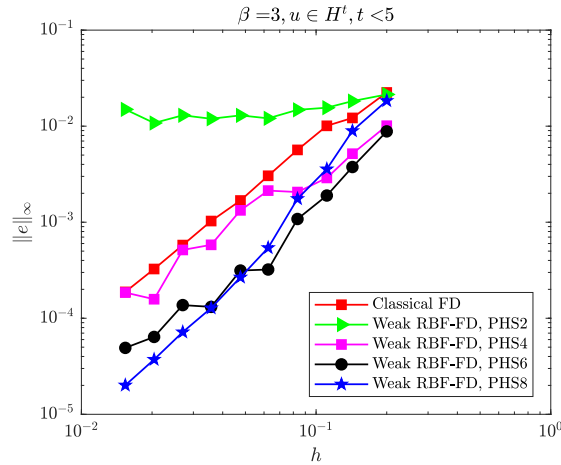


Figure 7: Comparing the absolute errors (discrete norm infinity) of the classical five-point star FD method with the weak-based RBF-FD method on regular points.

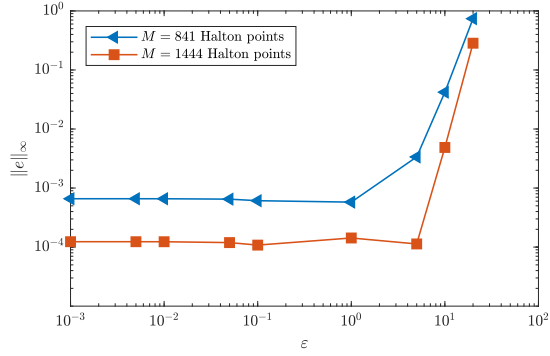


Figure 8: Absolute errors of the weak-based method as a function of  $\epsilon$  using GA kernel on two Halton sets.

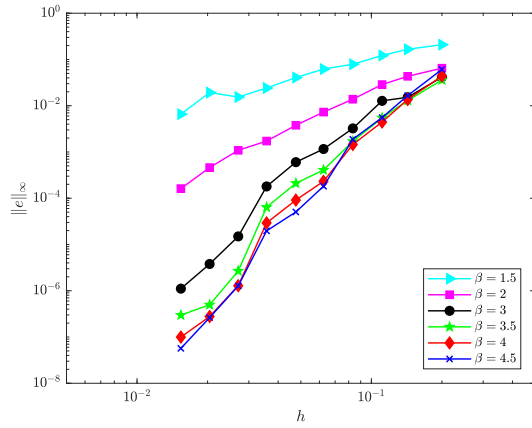


Figure 9: Convergence rates with respect to the smoothness of true solutions: the weak-based method with GA on regular points.

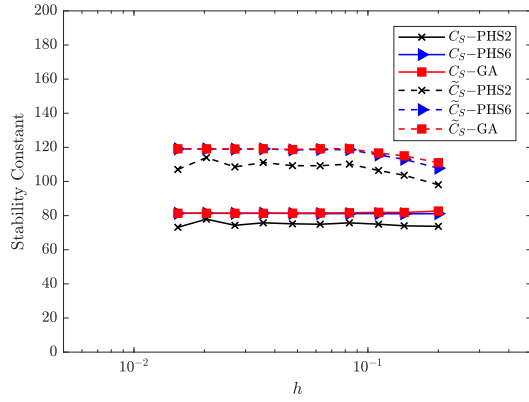


Figure 10: The growth of the stability constants  $C_S(A)$  and  $\tilde{C}_S(A)$  in terms of  $h$ ;  $A$  is the final matrix in (4.4).

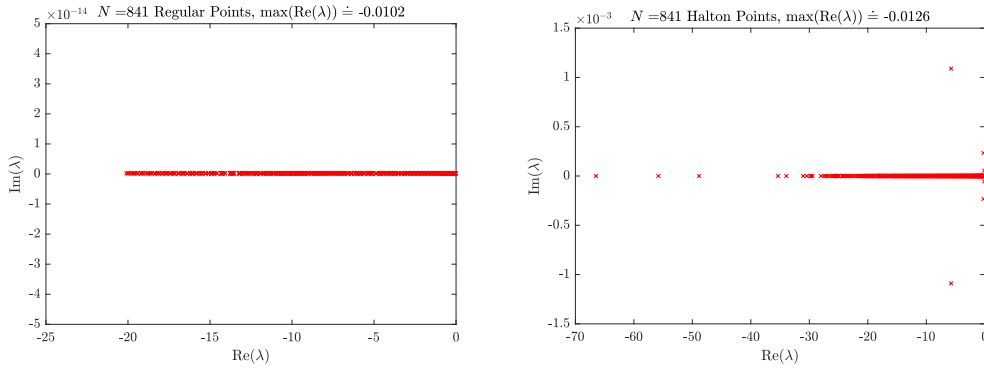


Figure 11: Spectrum of the discrete Laplacian by PHS2 kernel; regular (left) and Halton (right) points.

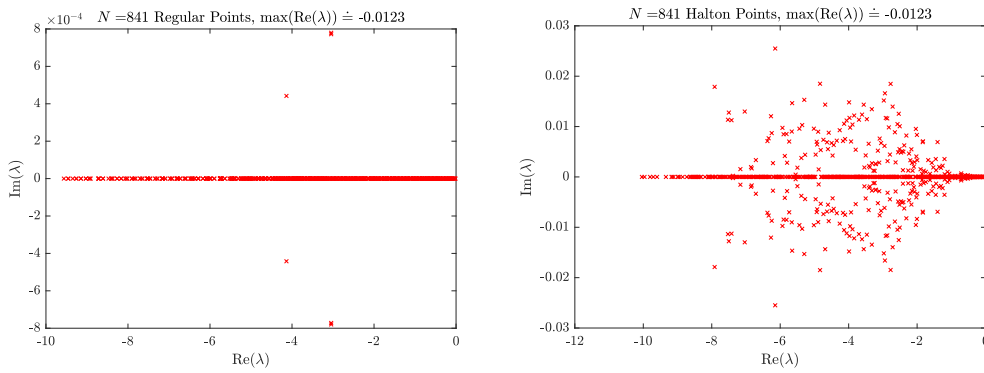


Figure 12: Spectrum of the discrete Laplacian by PHS6 kernel; regular (left) and Halton (right) points.

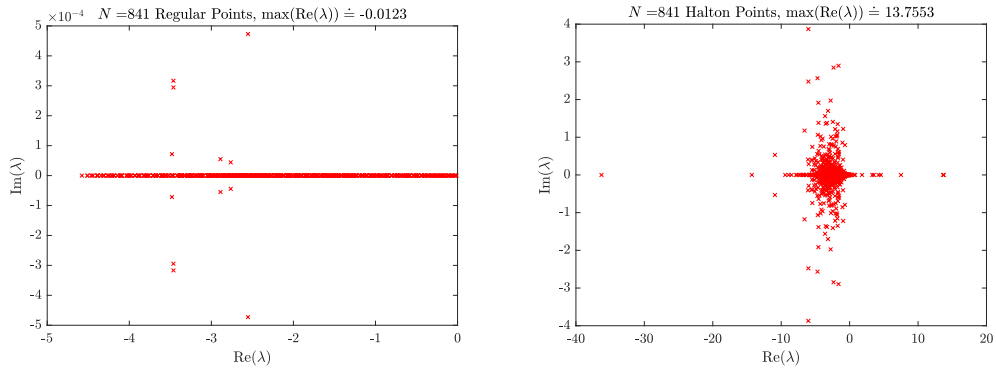


Figure 13: Spectrum of the discrete Laplacian by GA; regular (left) and Halton (right) points. Few eigenvalues have positive real parts on Halton points.

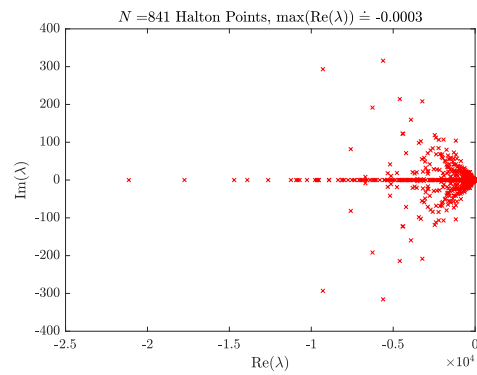


Figure 14: Spectrum of the discrete form of  $\Delta + \gamma_h \Delta^5$  where the Laplacian term is discretized by GA and the hyperviscosity term by PHS9; Halton points.

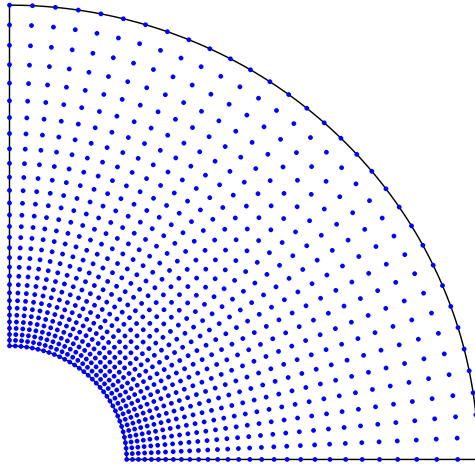


Figure 15: The computational domain of the elasticity problem and a set of 990 points.

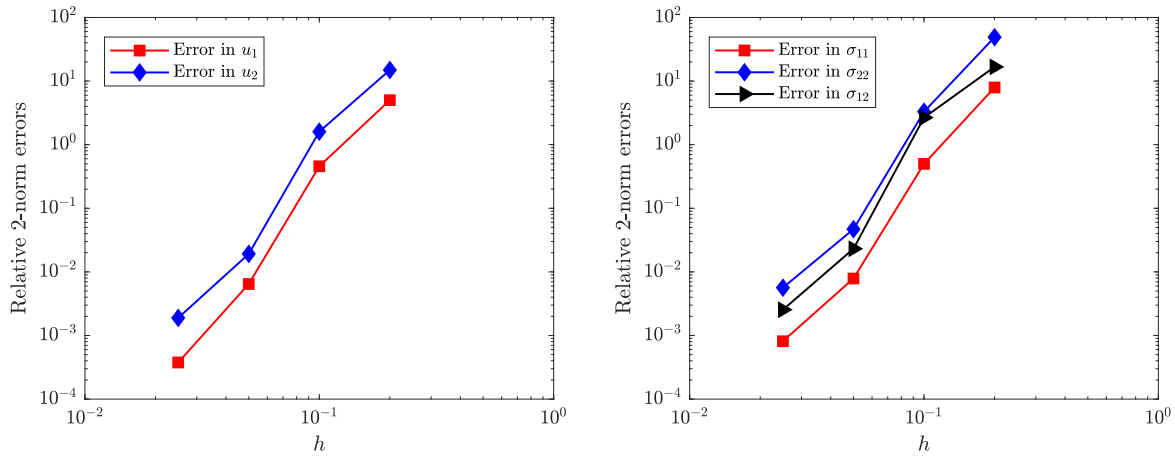


Figure 16: The relative discrete 2-norm errors of the displacement field (left) and normal/shear stresses (right) at different  $h$  levels.

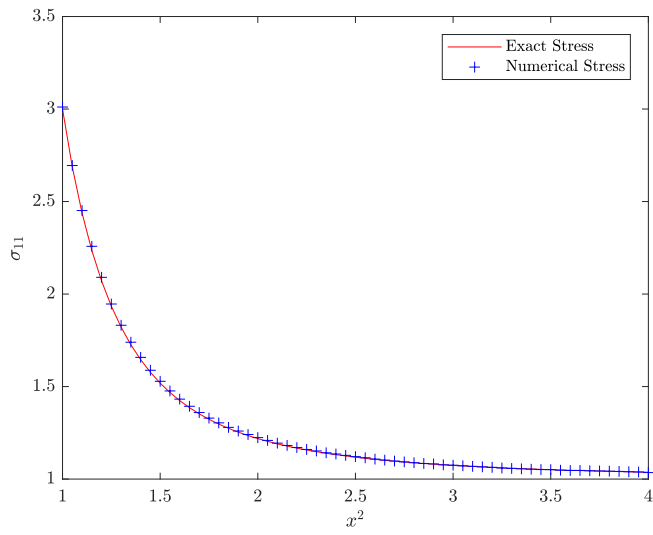


Figure 17: The exact normal stress  $\sigma_{11}$  at  $x^1 = 0$  compared with the numerical solution.